sustainability

Article

Impact of Land Cover Change on Mountain Circulation over the Hainan Island, China

Bingxue Wu [1], Junfeng Miao [1,*] and Wen Feng [2]

[1] College of Atmospheric Sciences, Nanjing University of Information Science and Technology, Nanjing 210044, China
[2] Hainan Meteorological Observatory, Haikou 570203, China
* Correspondence: miaoj@nuist.edu.cn

Abstract: Focusing on the complex underlying surface area in central–southern Hainan Island, this study uses the Advanced Research Weather Research and Forecasting Model (Version 4.0) to simulate a typical mountain circulation case without obvious weather system forcing, and tries to reveal the impacts of land cover changes on the mountain circulation. One control experiment (CNTL) and three sensitivity experiments, in which the current land cover is taken as areas of uniform evergreen broadleaf forest (FOREST), grassland (GRASS), and bare soil (DESERT) coverage, are conducted. The results show that the near-surface wind speed increases with decreasing surface roughness, and DESERT shows the most obvious change as compared with the CNTL. In the vertical direction, FOREST shows the strongest valley breeze circulation, with the largest horizontal and vertical extents of circulation, as well as the highest vertical extent of the updraft. DESERT shows the weakest valley breeze circulation with the longest duration. GRASS shows the slightest change from the CNTL. The possible impact mechanism is that the land cover changes could affect the surface energy partitioning, leading to a variation in the temperature distribution (i.e., the horizontal potential temperature gradient and boundary layer stability), in turn affecting the structure and evolution characteristics of the mountain circulation.

Keywords: complex terrain; local atmospheric circulation; land cover change; numerical simulation; tropical island

Citation: Wu, B.; Miao, J.; Feng, W. Impact of Land Cover Change on Mountain Circulation over the Hainan Island, China. *Sustainability* **2022**, *14*, 11794. https://doi.org/10.3390/su141811794

Academic Editor: Vilém Pechanec

Received: 11 June 2022
Accepted: 12 September 2022
Published: 19 September 2022

1. Introduction

The mountain circulation is defined as the local atmospheric circulation in mountainous areas. It mainly features mountain–valley wind circulation driven by the thermal contrast between the mountain atmosphere and the surroundings, which comprise the slope flow, along-valley wind, and mountain–plain wind circulation [1]. When the synoptic forcing is weak, the wind direction generally reverses twice a day, affected by the mountain–valley wind. Depending on the ground cover conditions, however, the mountain–valley wind circulation can interact with other small- and meso-scale circulations such as sea–land breeze [2], lake–land breeze [3], and urban heat island circulation [4], showing more complicated circulation characteristics. The mountain circulation has a great effect on the near-surface flow regime, boundary layer structure, local climate, air pollution transport and diffusion, and trigger of the convection and precipitation [5–9]. The mountain circulation varies greatly from place to place, with different strengths, depths, levels of persistence, and onset times, depending on the terrain characteristics, land cover, soil moisture, insolation, local shading, and surface energy budget [10].

Due to human activities and climate change, the land cover types have undergone significant changes in many regions of the world, and these changes will only continue in the future. Studies have shown that land cover changes can alter the spatiotemporal distribution of atmospheric variables, resulting in far-reaching impacts on the local weather and regional climate [11–13]. Land cover changes have also been shown to modify the mountain circulation by affecting the surface roughness, near-surface temperature and humidity, and boundary layer characteristics [14]. For example, Zhang [15] used idealized modeling experiments and showed that a larger vegetation coverage results in the later formation of mountain–valley breeze circulation with weaker intensity and shorter duration. Gross [16] noted that deforestation can enhance nighttime atmospheric stability as the inversion layer drops from treetop height to near the ground. Chu et al. [17] pointed out that the mountain breeze circulation weakens after mountain-slope afforestation in Lanzhou because of the reduced surface thermal heterogeneity. Letcher and Minder [18] investigated the response of the mountain circulation in the Rocky Mountains to snow cover reduction under climate warming, and an intensified plain breeze circulation is presented, which favors the accumulation of pollution concentration within the mountain boundary layer, owing to the increasing thermal contrast. Wang et al. [19,20] conducted three sensitivity experiments in which the original land cover map of Huangshan Mountain was modified by uniform forest, grass and bare soil, respectively. Their results showed that the heat fluxes change most significantly in the bare soil experiment, as does the corresponding flow field.

The Hainan Island (18.16° N–20.17° N, 108.61° E–111.05° E) is located to the south of mainland China. In the tropical zone, the island receives sufficient insolation. Two mountain ranges, the Limu Mountain and Wuzhi Mountain, occupy the south–central part of the island, with a diameter of roughly 160 km and a peak altitude of roughly 1.8 km. The corresponding lands are mainly covered by cropland and evergreen broadleaf forest on the plain and mountain slope. Under such unique terrain and geographical location, the local atmospheric flow field is significantly affected by mesoscale circulations such as sea-land breeze and mountain–valley breeze, which often trigger convection [21,22]. Previous researchers have provided insight into the structure and evolution of the sea–land breeze over Hainan Island [23–25], and pointed out that the effect of the terrain features on the sea breeze is dramatic [26–28]. However, few studies have paid close attention to the mountain–valley circulation on this island.

In 2019, China's central government launched the project of constructing the Hainan Tropical Rainforest National Park System Pilot Area to promote ecological progress, and some policies and measures have just begun to be implemented. Furthermore, by comparing the simulations of near-surface meteorological fields in Hainan Island using the new high-resolution land and WRF default land surface data (land use, vegetation fraction, terrain, and soil type), Zhang et al. [29] found that simulations using the new land cover dataset produces more pronounced change.

Motivated by the above reasons, this study focuses on the complex underlying surface in south–central Hainan Island and aims to reveal the impacts of land cover changes on the structure and evolution of the mountain circulation through high-resolution numerical simulations. The remainder of this paper is organized as follows. Section 2 describes the data and study case. The model setup and experiment design are presented in Section 3. In Section 4, the simulation results are validated by comparing them with the observations. A detailed analysis of the simulation results is given in Section 5. Section 6 presents the conclusions.

2. Data and Case Description

The data used in the case selection and model validation include the hourly surface observation data, the sounding data for Sanya station, the hourly satellite cloud image data from the website of the Environment College of The Hong Kong University of Science and Technology, and the hourly fifth-generation ECMWF atmospheric reanalysis data (ERA5) with a spatial resolution of $0.25° \times 0.25°$.

The case of 1–2 May 2020 is selected for this study because of the weak gradient wind and fair weather conditions, which are favorable for the development of local circulation [22]. According to the synoptic situation at 08:00 LST (local standard time UTC+8, the same below) at 500 hPa, Hainan Island is located in the northwest portion of the West Pacific subtropical high and surrounded by the 588 dagpm isoline. At both 700 hPa (Figure 1a) and 850 hPa, Hainan Island is governed by a 2–4 m/s southerly wind. There is no observed cloud system formation over the island (Figure 1b) and no precipitation at surface meteorological stations.

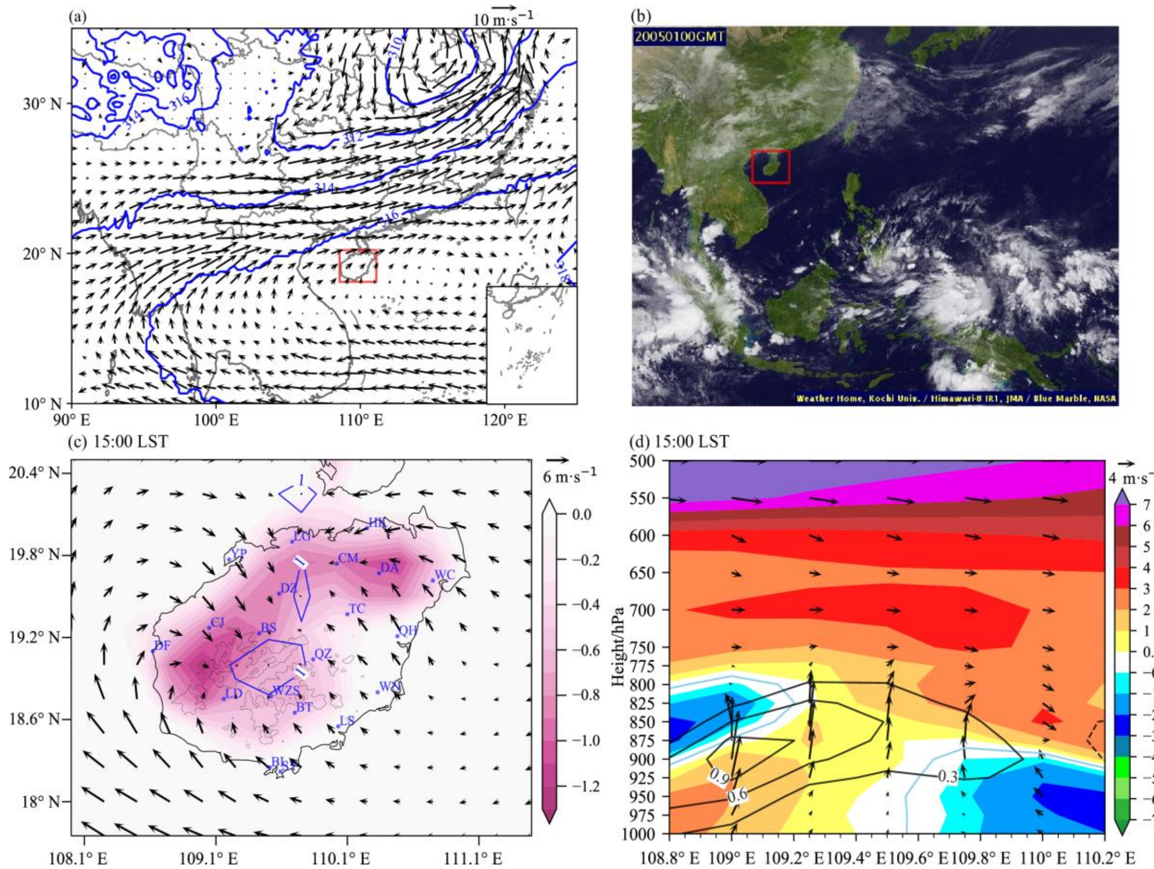

Figure 1. (**a**) The 700 hPa circulation field analyzed via ERA5 data and (**b**) cloud images obtained using the Himawari-8 satellite (http://envf.ust.hk/dataview/geo_sat_map/current/index.py?maptype__string=KOCHI_GEO_MAP accessed on 17 December 2021) at 08:00 LST 1 May 2020. (**c**) The 975 hPa wind and divergence field and (**d**) vertical circulation along 19° N analyzed using ERA5 data at 15:00 LST. (**a**) The vector indicates the wind field, the blue contour line is the geopotential height (units: dagpm), and (**a**,**b**) the red rectangular area shows the Hainan Island. (**c**) The vector indicates the wind field, the shading is the divergence (units: 10^{-4} s^{-1}), and the blue contour line is the wind velocity isoline of 1 m/s. (**d**) The vector indicates the (u, -ω) wind field, where the ω (unit: Pa/s) is multiplied by 10; the shading shows the zonal wind and the thin black isoline is the vertical velocity.

The wind sounding data from SY station show that the speed of the wind below 500 hPa is less than 8 m/s. The surface observation data show that the wind at stations near the mountain shift to move up slopes around noon time. In addition, the ERA5 data show that the mountain area is affected by local circulation in the afternoon, which is characterized by inward flow towards the mountain range (Figure 1c), as well as a circulation that appears on both sides of the mountain area (Figure 1d). Furthermore, the near-surface wind field characteristics of this case are quite similar to the results [21] shown by the observational statistical analysis that the wind field tends to converge towards the center of the mountain area with time. In short, this day can be regarded as a typical mountain circulation case for in-depth study.

3. Mode Setup and Experiment Design

The Weather Research and Forecasting Model (WRF-ARW version 4.0; https://www2.mmm.ucar.edu/wrf/users/docs/user_guide_v4/contents.html accessed on 17 December 2021) is utilized for the numerical simulation, and two-way feedback, quadruply-nested grid is configured. The nested domains (D1–D4) have (x, y) dimensions of 200 × 200, 208 × 202, 184 × 190, and 241 × 226, with grid spacings of 27, 9, 3, and 1 km, respectively. The coarse domain (D1) encompasses most of East Asia, while the finer domain (D4) covers central and southern Hainan Island (Figure 2a). In the vertical section, all four domains consist of 36 σ-levels ranging from the ground to 100 hPa, with 22 levels below 2 km, so as to better capture the atmospheric boundary layer characteristics. The topography information (Figure 2b) is derived from the United States Geological Survey Global Multi-Resolution Terrain Elevation Data (USGS GMTED2010; https://www.usgs.gov/coastal-changes-and-impacts/gmted2010 accessed on 17 December 2022). The land use information (Figure 2c) is from the Moderate-Resolution Imaging Spectroradiometer (MODIS) databases, with spatial resolutions of 10, 5, and 2 arc-min and 30 arc-sec for D1, D2, D3, and D4, respectively. The physical parameterizations used in this study are summarized in Table 1. The initial and boundary conditions are provided by the 6-hourly 0.25° × 0.25° resolution National Centers for Environmental Prediction Final Global Analysis (NCEP FNL) data. The simulation integrates data from 08:00 LST on 30 April 2020 to 08:00 LST on 2 May 2020, and outputs data hourly. The first 24 h period is discarded as the spin-up time, and the following 24 h period is considered for the analysis.

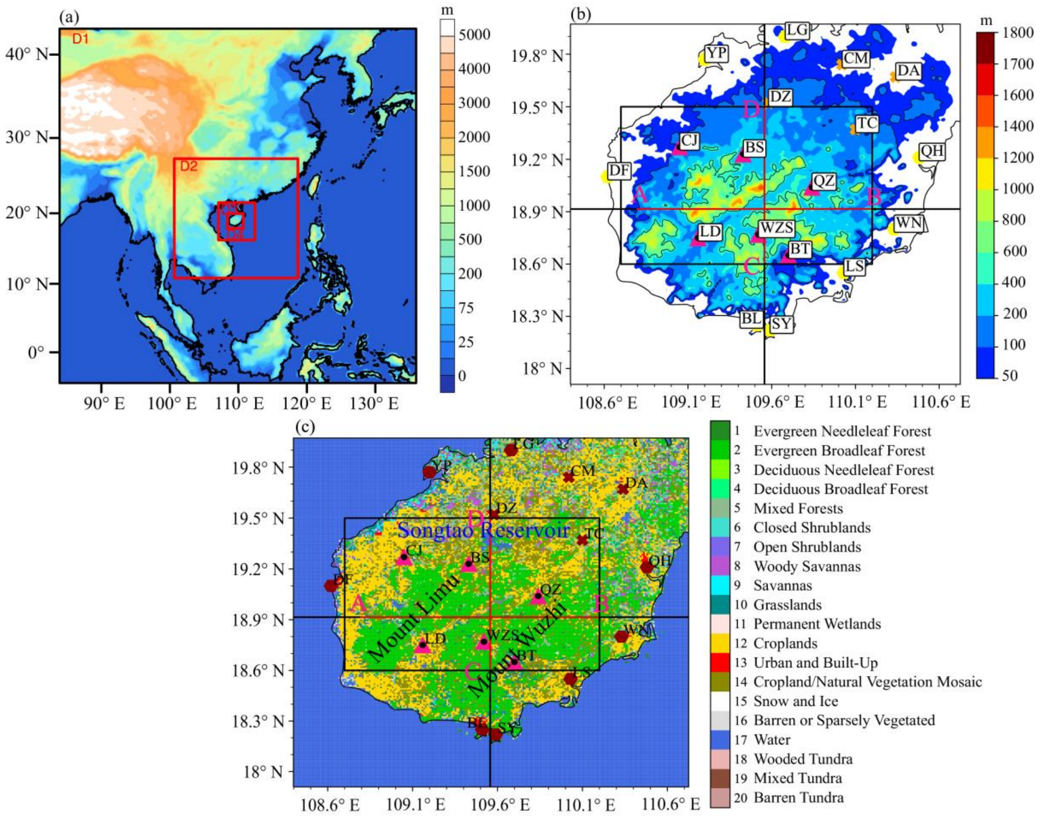

Figure 2. (**a**) Coverage of model domains. (**b**) Terrain height and the distribution of meteorological stations in the innermost domain (D4). (**c**) Land use types in D4. Line AB and CD (**b**) indicate the location of the vertical cross-section used in this study, and the rectangular areas (**b**,**c**) represent the mountain area of interest. Abbreviations of the meteorological stations: DF: Dongfang; YP: Yangpu; LG: Lingao; QH: Qionghai; WN: Wanning; LS: Lingshui; SY: Sanya; BL: Bailu; DZ: Danzhou; CM: Chengmai; DA: Dingan; TC: Tunchang; LD: Ledong; CJ: Changjiang; BS: Baisha; QZ: Qiongzhong; WZS: Wuzhishan; BT: Baoting.

Table 1. Settings of the main physical parameterizations.

Physics Process	Parameterization Option
Shortwave radiation	RRTMG
Longwave radiation	RRTMG
Microphysical process	Lin
Cumulus (only in D1, D2)	Kain-Fritsch
Boundary Layer	YSU
Surface Layer	MM5
Land surface process	Noah

To identify the impacts of land cover changes on the mountain circulation directly, a series of sensitivity tests are designed by replacing vegetation types in the innermost domain (D4), similar to Miao et al. [20] and Wang et al. [30]. The run using the real topography and vegetation types is regarded as the control experiment (CNTL). In contrast, the other three sensitivity experiments are identical to the CNTL, except for changes in vegetation type (Table 2). The other three sensitivity experiments mainly modify the vegetation type variable (LU_INDEX) and vegetation coverage variable (LANDUSEF) of the static data (geo_em.d04.nc) from the WRF Preprocessing System (WPS).

Table 2. Scenarios of numerical experiments.

Experiment	Vegetation Type
CNTL	Heterogeneous land cover (MODIS data)
FOREST	Homogeneous land cover (evergreen broadleaf forest)
GRASS	Homogeneous land cover (grassland)
DESERT	Homogeneous land cover (bare soil)

4. Comparison with Observations

The six stations near the mountain (CJ, BT, BS, LD, QZ, WZS) are selected to evaluate the model performance and understand the basic characteristics of the mountain–valley wind. Figures 3–5 show the diurnal variations in 2 m temperature, 10 m wind speed, and wind direction, and the simulation results are used from the grid point closest to each station. As shown from the observations at all stations, the temperature starts increasing soon after sunrise and reaches the maximum at around 15:00 LST. After this, the temperature drops rapidly and the cooling rate tends to be lower at night. The WRF model slightly underestimates the temperature, with a limit of about 2 °C, but reproduces the diurnal variation in temperature well.

The diurnal characteristics of the wind field vary significantly with the different local topographical features [31]. CJ and BT stations (Figure 3), which are located at the northwest and southeast sides of the mountain range, exhibit the mountain–valley wind characteristics clearly. For instance, two almost opposite shifts in wind direction can be observed around 09:00 and 21:00 LST, indicating the beginning and end of the valley wind period, which brings higher wind speeds. BS and LD stations (Figure 4) are located to the north and the south of Limu Mountain. A clear diurnal cycle of the wind field can be observed at BS station, with strong northerly valley wind during the day and much weaker wind during the night, while the southwesterly wind persists at LD station after 15:00 LST, parallel to the northeast–southwest oriented valley. QZ and WZS stations (Figure 5) are located to the north of Wuzhi Mountain and on the west–east valley axis between the north and south sections of Wuzhi Mountain, respectively. The observed wind direction of the two stations is easterly wind throughout the day because of the existence of the low-level easterly background wind.

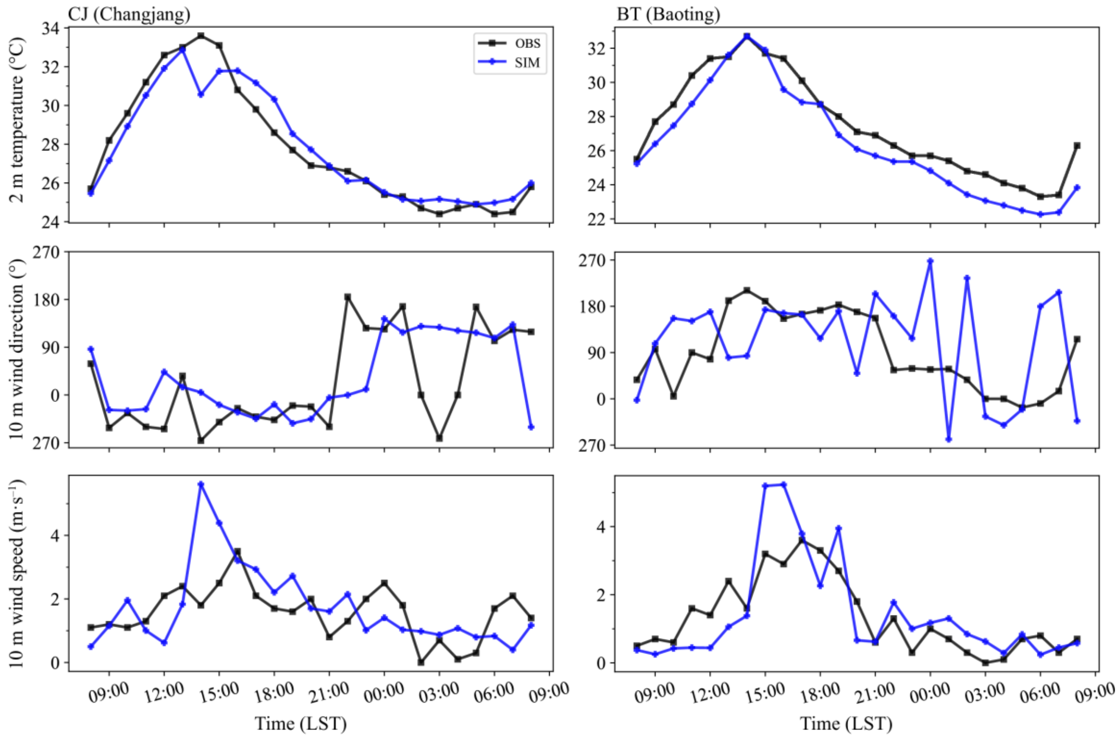

Figure 3. Comparisons between the simulated and observed 2 m temperature (**top**), 10 m wind direction (**middle**), and 10 m wind speed (**bottom**) values at CJ and BT stations from 08:00 LST on May 1 to 08:00 LST on May 2, 2020. The black lines and blue lines indicate the observation and simulation, respectively.

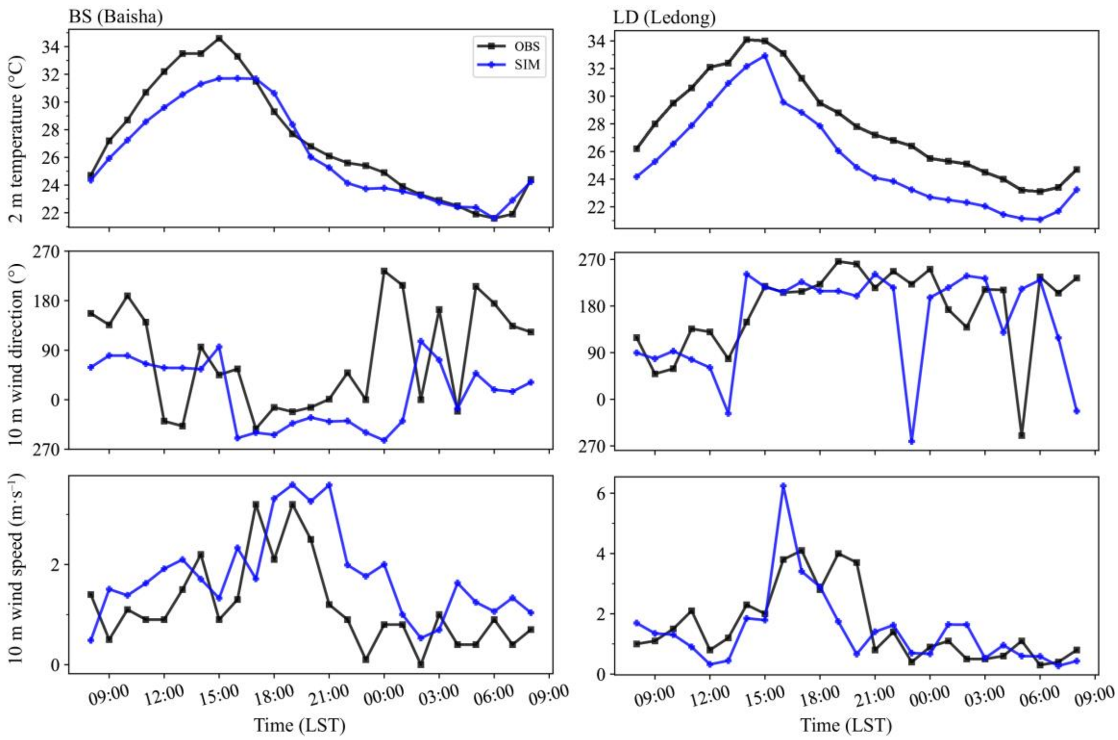

Figure 4. Comparisons between the simulated and observed 2 m temperature (**top**), 10 m wind direction (**middle**), and 10 m wind speed (**bottom**) values for BS and LD stations.

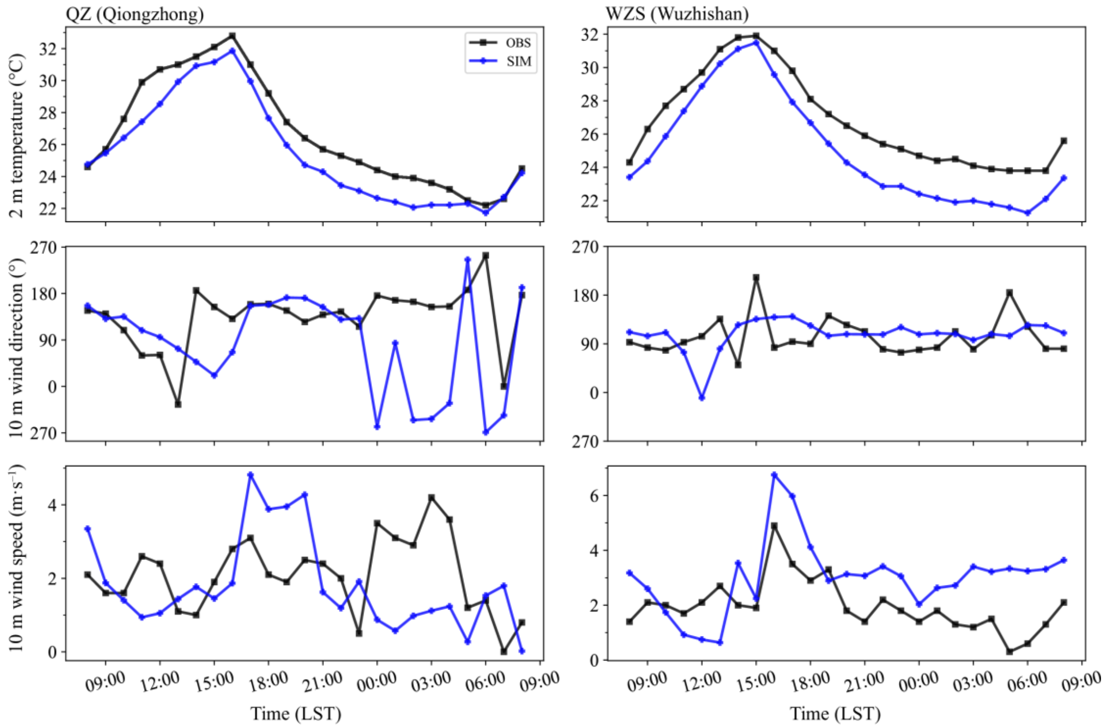

Figure 5. Comparisons between the simulated and observed 2 m temperature (**top**), 10 m wind direction (**middle**), and 10 m wind speed (**bottom**) values for QZ and WZS stations.

The simulated variation trends of the wind speed and wind direction are in good agreement with the observations, while the maximum wind speed in the afternoon is overestimated. In addition, the wind direction deviation is larger at night, which may be attributed to the changeable wind direction associated with the low wind speed.

The analysis above confirms that the WRF simulation can reflect the main features of the mountain circulation with acceptable deviations.

5. Results and Discussion

5.1. Horizontal Structure

Figure 6 shows the horizontal wind field at 15:00 LST. As can be seen for the CNTL (Figure 6a), a well-defined valley wind is captured, consisting mainly of the upslope wind (2–3 m/s) on the sloping mountain and the plain wind (4 m/s) outside the mountain, which is characterized by a significant convergence tendency towards the center of the mountain area. When the underlying surface is replaced by uniform areas of forest, grass, and bare soil, the flow field is still dominated by valley wind, but compared with the CNTL, there are some wind speed changes to different degrees. Specifically, the plain breeze is weaker with a weak divergence flow appearing at the edge of the mountain for FOREST (Figure 6b). The change of wind speed is slight in GRASS (Figure 6c), while the wind becomes stronger in DESERT (Figure 6d). Therefore, it can be inferred that the near-surface wind speed increases with the decreasing height and coverage area of the vegetation due to the reduced surface roughness length. This is consistent with Cheng et al. [32], who reported that the roughness length is a key parameter affecting the wind speed over Taiwan Island. Moreover, a significant easterly wind component occurs at the western edge of the mountain in the three sensitivity experiments, indicating that the penetration distance of the westerly plain wind is shortened. Among them, the plain breeze is blocked mostly for DESERT, with its easterly component having a greater intensity and extension. It is also noted that that convergence of flow at Songtao Reservoir strengthens after the change in underlying surface. An explanation for this phenomenon may be that the air temperature can rise by 3–4 °C after the water from Songtao Reservoir is replaced by vegetation, meaning the horizontal land–water temperature contrast diminishes, weakening the divergence originally caused by the lake breeze.

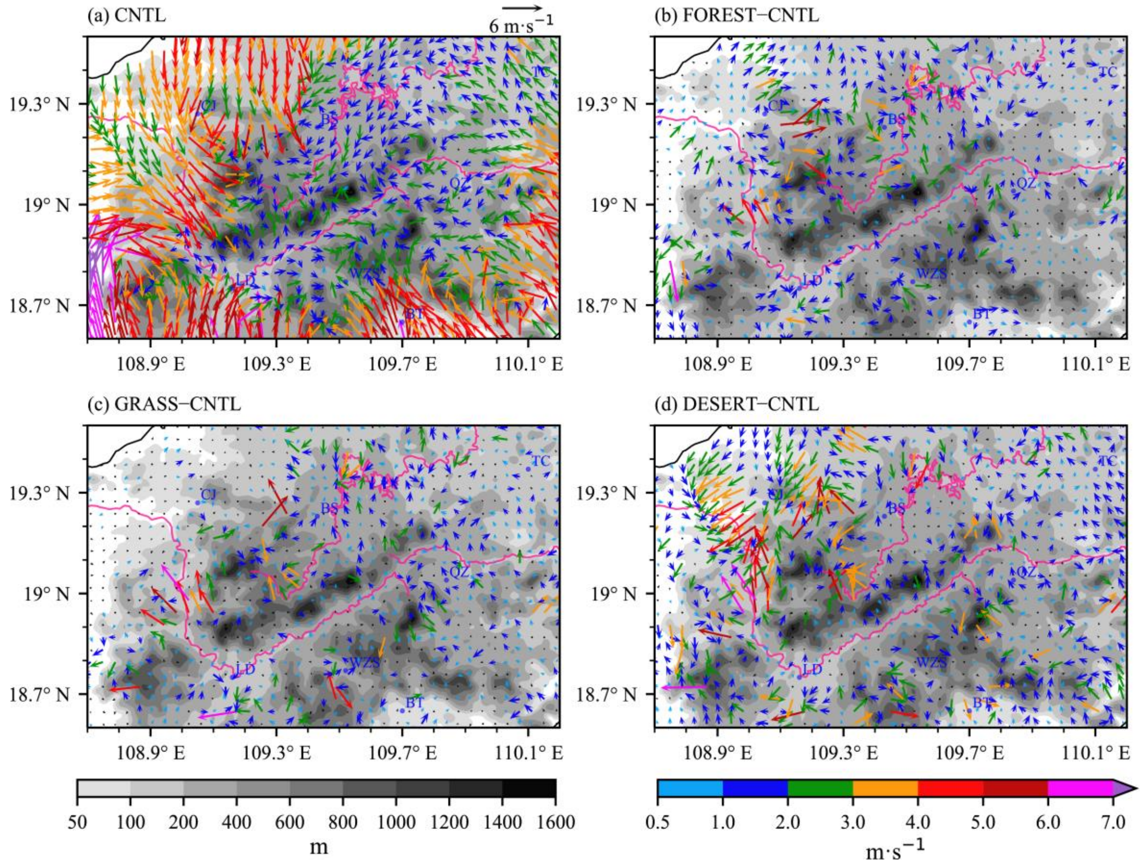

Figure 6. (**a**) Simulated 10 m wind field of the CNTL and (**b**–**d**) the difference in 10 m wind fields between the three sensitivity experiments and the CNTL at 15:00 LST. The vector indicates the wind field, with the color representing the wind speed, while the pink line indicates the river. The shading represents the terrain in the model.

To better understand the evolution of the near-surface wind field under the different land cover situations, the temporal variations in the 10 m wind field along 18.92° N (line AB in Figure 2b) and 109.56° E (line CD in Figure 2b) are shown in Figures 7 and 8, respectively.

For the CNTL in the west–east direction (Figure 7a), the plain wind and upslope wind are established at around 10:00 LST. Then, the upslope flow is enhanced and the plain wind penetrates toward the center of the mountain area gradually with the persistent solar heating. The plain breeze peaks at around 16:00 LST. By around 19:00 LST, the wind direction starts to reverse as the mountain wind appears, and the wind speed increases substantially after midnight, especially on the west side of Limu Mountain. After the forest area expands (Figure 7b), the greatest change in wind field occurs in the western plain, where the wind speed slows down by about 1 m/s over a whole day. There is a relatively small change in GRASS (Figure 7c), and the difference is more apparent from 14:00 to 18:00 LST. For DESERT (Figure 7d), the wind speed increases obviously, especially the valley wind, which is increased by about 2 m/s from 16:00 to 18:00 LST. The duration of the valley wind is also extended by 2 h to 20:00 LST, and its peak is postponed to around 18:00 LST.

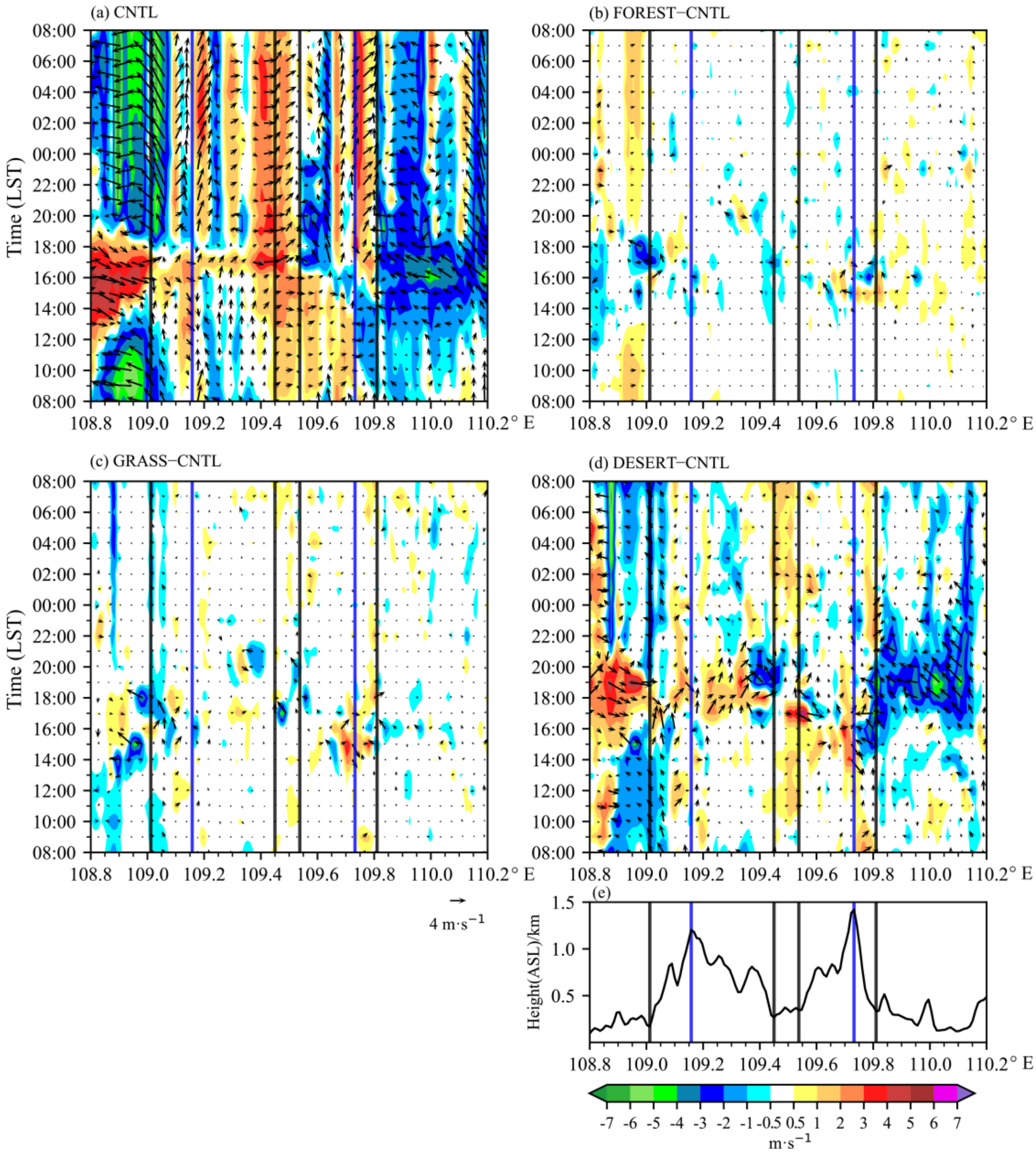

Figure 7. (**a**) The evolution of the simulated 10 m wind field caused by the CNTL along the line AB from Figure 2b. (**b**–**d**) The differences in 10 m wind fields between three sensitivity experiments and the CNTL. (**e**) Terrain height along the line AB from Figure 2b. The vector indicates the wind field, the shading shows the zonal wind, the blue vertical lines indicate the tops of the mountains, and the black vertical lines indicate the bases of mountains.

For the CNTL in the south–north direction (Figure 8a), similar to the west–east direction, the flows converge sharply along mountain ridges, and the speed reaches the maximum at about 16:00 LST. However, the south–north valley wind is maintained for longer than that on the west–east direction. At 19:00 LST, the plain wind on the northern plain begins to develop, while the valley winds on the north and south sides propagate further and converge at 19.23° N at 20:00 LST. After 20:00 LST, the mountain wind develops, causing weakened wind on the northern plain and strengthened wind on the northern slope of the mountains. For FOREST (Figure 8b), the area of change is mainly located in the northern plain, where the wind speed decreases during the daytime (11:00–18:00 LST), while the strength and penetration distance of the plain wind increase at night (19:00–20:00 LST). For GRASS (Figure 8c), the southerly wind increases slightly during 11:00–18:00 LST. For DESERT (Figure 8d), there is a great difference during 16:00–22:00 LST, whereby the valley wind is 2 m/s larger than the CNTL integrally, and mostly at 19:00 LST. In addition, the three sensitivity experiments all show that the northerly components larger than 2 m/s appear near 19.4° N for just the Songtao Reservoir before sunset, indicating that the northerly wind could advance southward further after the lake breeze weakens.

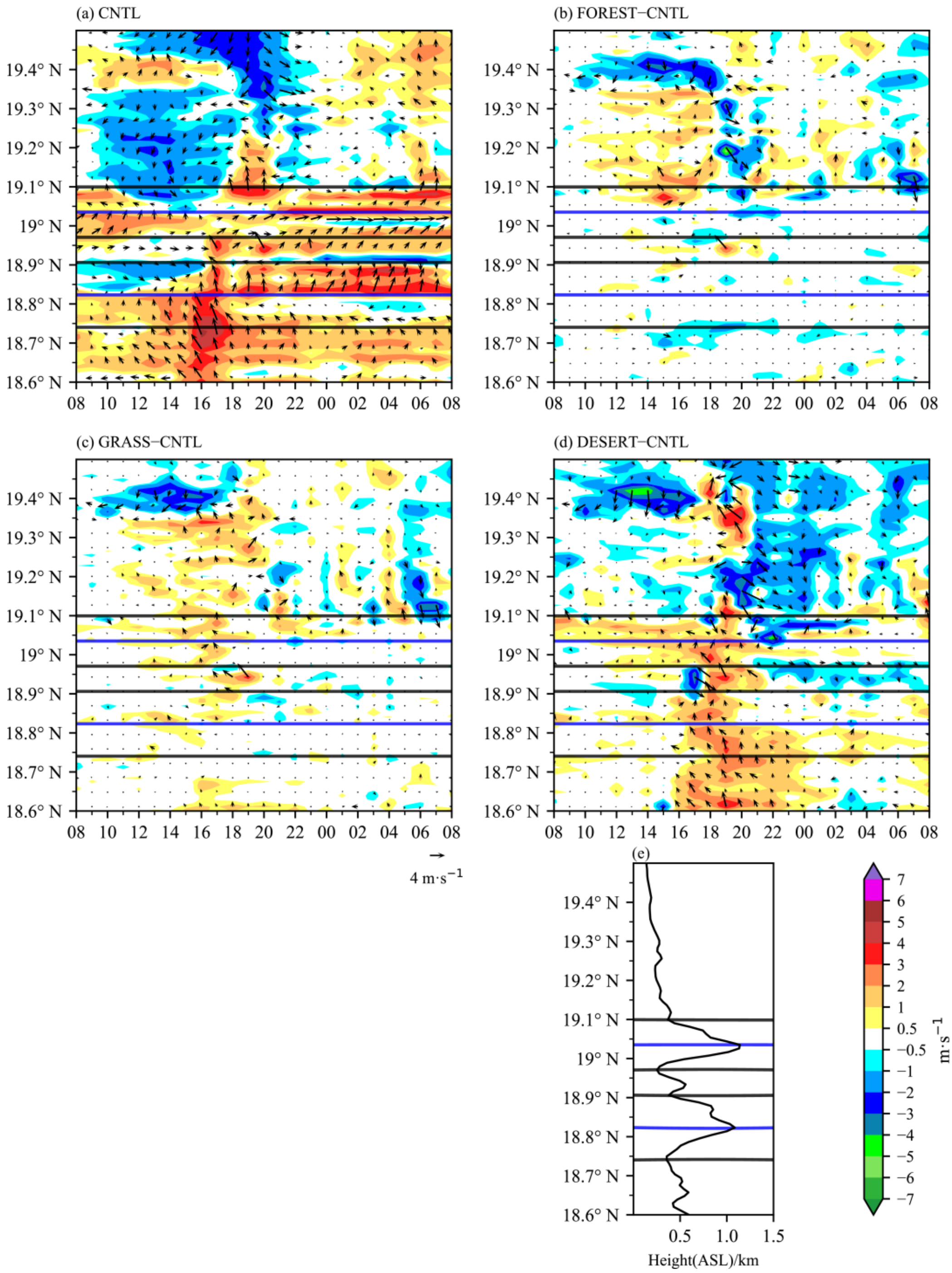

Figure 8. The evolution of the simulated 10 m wind field caused by the CNTL along the line CD from Figure 2b.

5.2. Vertical Structure

Figures 9 and 10 show the vertical cross-sections of the wind field, potential temperature, and PBL height along the west–east (line AB in Figure 2b) and south–north (line CD in Figure 2b) directions at 15:00 LST, respectively. Figures 11 and 12 are the same as

Figures 9 and 10, but for 17:00 LST. For the CNTL (Figure 9a), the plain and upslope wind circulations are evident in the west–east section, corresponding to the horizontal wind patterns (Figure 9a). The upward motion is strong at the leading edge of the circulation.

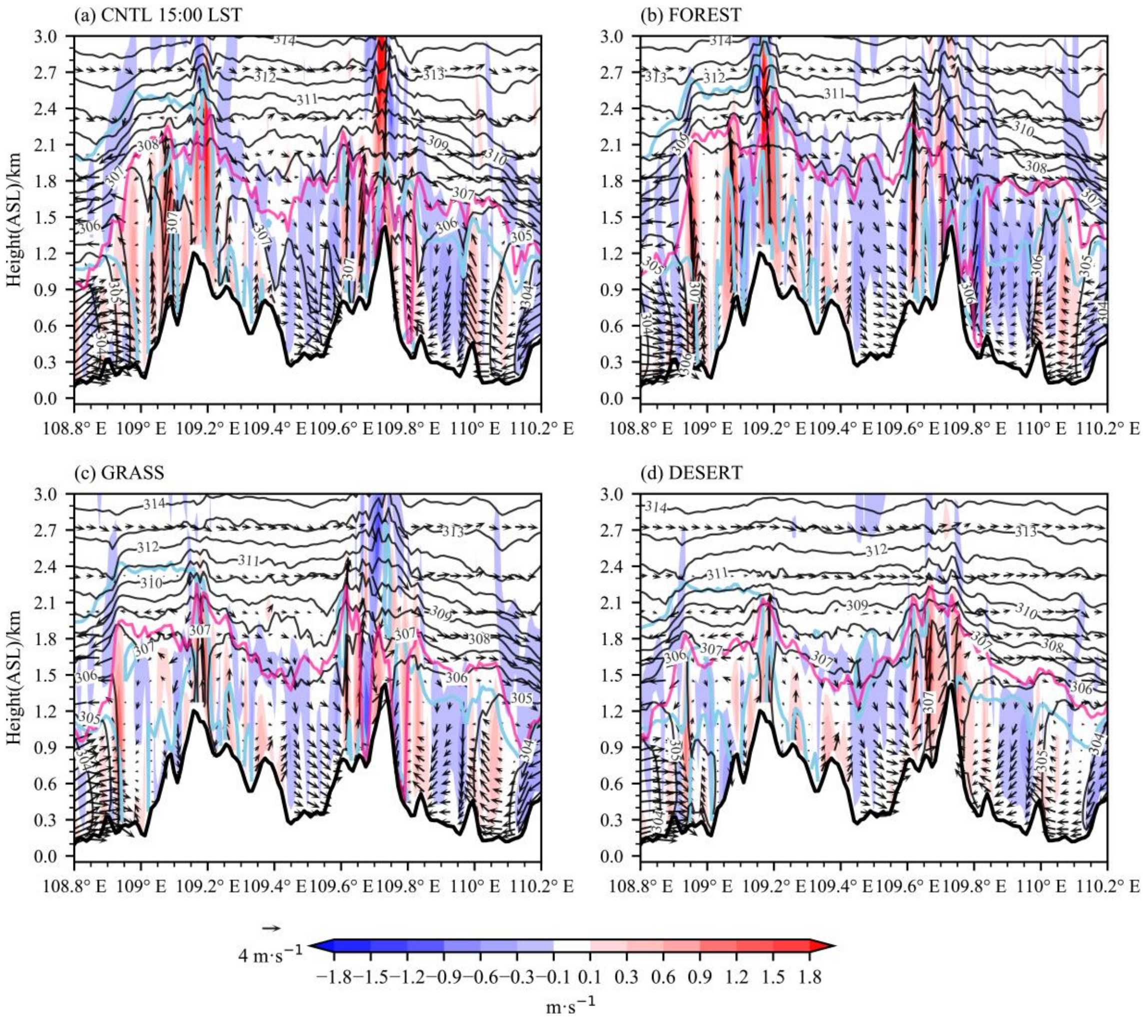

Figure 9. Simulated vertical circulations and distributions of the potential temperature and planetary boundary layer height along line AB from Figure 2b for the four experiments at 15:00 LST: (**a**) CNTL, (**b**) FOREST, (**c**) GRASS and (**d**) DESERT. The vector (u, w) indicates the wind field with the w-component multiplied by 10. The shading shows the vertical velocity, the blue contour line denotes the zero u wind speed, the black contour line is the potential temperature, the red line is the planetary boundary layer height, and the thick black line indicates the terrain.

The scale of the valley wind circulation varies with the altered land cover. Specifically, the western plain wind penetrates to 108.98° E for the CNTL and FOREST, and to 108.94° E for GRASS and DESERT, at 18 km and 14 km toward inland, respectively. The depths of the western plain wind (about 0.9 km AGL) are almost the same in the four experiments, while the depth of western upslope wind for GRASS and DESERT is only 0.3 km, which is much shallower than those for the CNTL and FOREST. The upward motion on the west side is prominent for FOREST, as exhibited by three strong updrafts up to nearly 2 km ASL, and the maximum upward velocity among them can reach 2.6 m/s, which is 0.3 m/s larger than for the CNTL. However, the maximum velocity and vertical extent of the updrafts are weaker for GRASS and DESERT compared to the CNTL, and it is more obvious for DESERT, being 0.3 m/s smaller and 400 m lower, respectively.

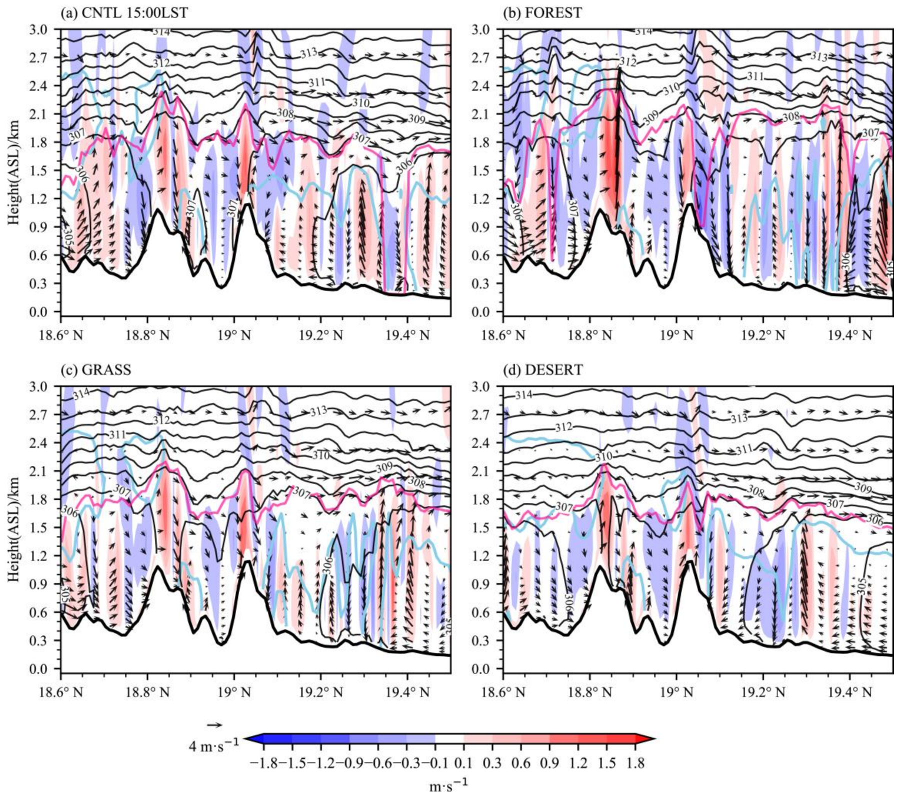

Figure 10. Simulated vertical circulations and distributions of the potential temperature and planetary boundary layer height along line CD from Figure 2b for the four experiments at 15:00 LST.

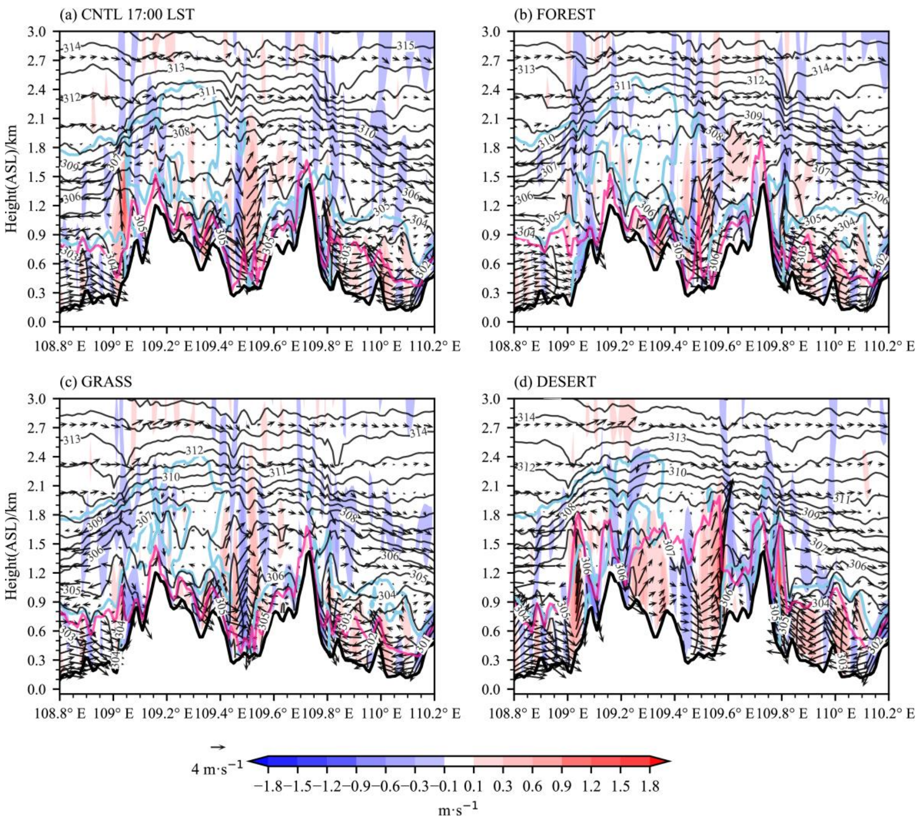

Figure 11. Simulated vertical circulations and distributions of the potential temperature and planetary boundary layer height along line AB from Figure 2b for the four experiments at 17:00 LST.

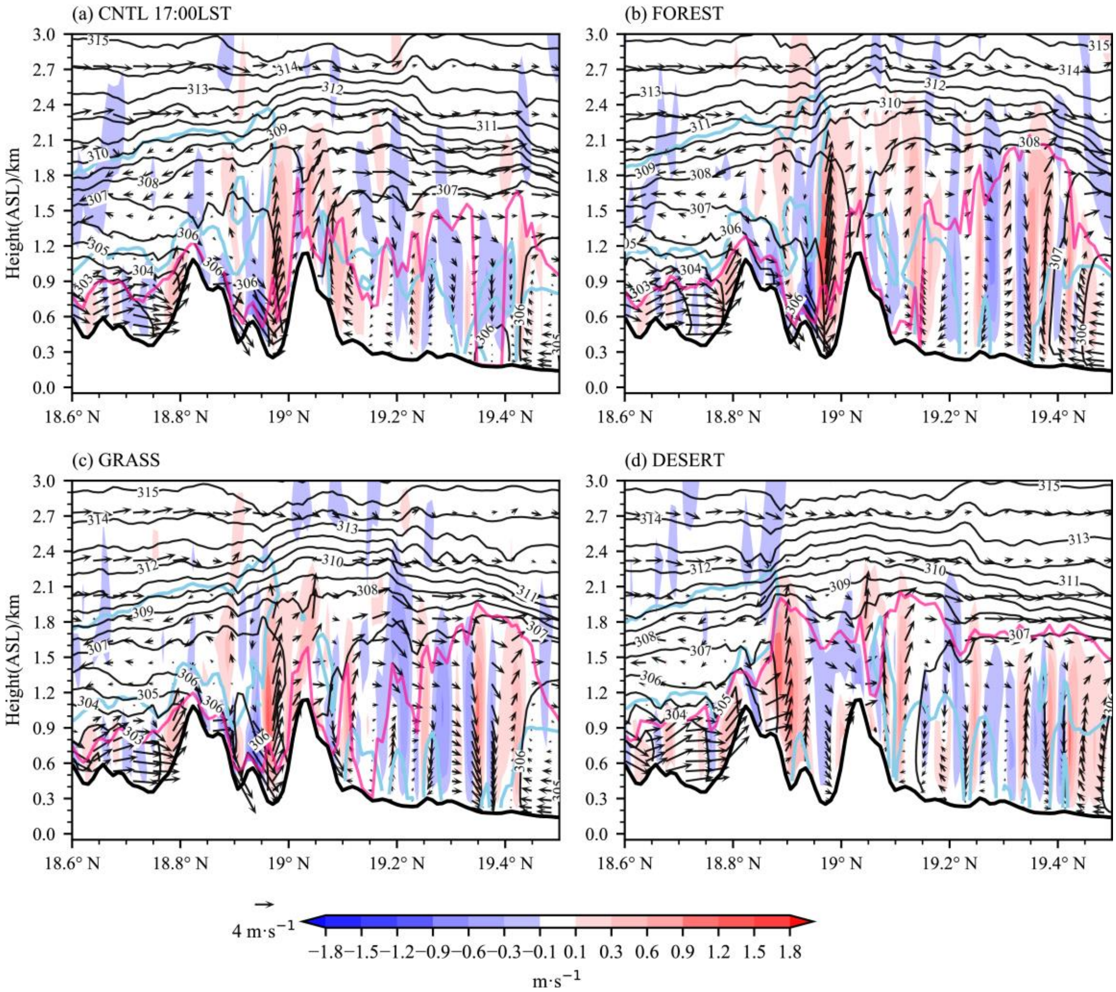

Figure 12. Simulated vertical circulations and distributions of the potential temperature and planetary boundary layer height along line CD from Figure 2b for the four experiments at 17:00 LST.

On the east side, the plain wind is combined with the upslope wind, moving westward together. The penetration distances are 57 km (FOREST), 53 km (CNTL), 44 km (GRASS), and 42 km (DESERT), respectively. Among them, the valley wind for FOREST and the CNTL can cross the top of Wuzhi Mountain, while those for GRASS and DESERT only reach near the mountaintop. The height of the valley wind for DESERT is about 0.1 km shallower than for the other three experiments. The maximum upward velocity values are 2.7 m/s (CNTL), 2 m/s (FOREST), 1.7 m/s (GRASS) and 1.7 m/s (DESERT), respectively. It is noted that for DESERT, the strength upslope flow on the western slope of Wuzhi Mountain is stronger with a larger horizontal extension of ascending motion due to being less affected by the valley wind on the east of the mountain, but the vertical extension is still lower than for the other experiments.

In the south–north section at 15:00 LST (Figure 10), comparing the southern circulations of the four experiments, it can be seen that the plain and upslope wind circulations are the most pronounced for FOREST; the wind speed and updraft velocity are stronger and the upslope wind can extend to about 1 km AGL, whereas the circulations are weakest for DESERT and the depth of the upslope wind is about 0.4 km thinner than for FOREST. Only slight differences can be seen between GRASS and CNTL. In the north of the mountain area, compared to the CNTL, the boundary layer height near 19.4° N is higher and the plain wind advance 5–10 km further south for the three sensitivity experiments. This means that the plain breeze advances further after the water disappears, which is consistent with the conclusion shown in the previous horizontal circulation map and further confirms the blocking effect of the lake breeze near Songtao Reservoir.

In the west–east section at 17:00 LST (Figure 11), the valley winds from both sides of the mountain can penetrate as far as the valley center, and the accompanying two updrafts finally merge with each other. It is noted that a decrease in boundary layer height at this time is evident as compared with 15:00 LST, particularly over the mountains, which acts to inhibit the development of upward motion [33]. For all experiments, the differences are mainly presented in the upward motion. Compared with the CNTL, the ascending velocity values for FOREST and GRASS weaken, and the decrease can reach 1 m/s in the western foothills of Limu Mountain. In contrast, the boundary layer is much deeper, and accordingly the ascending velocity intensifies for DESERT.

In the south–north section at 17:00 LST (Figure 12), a larger circulation can be found in the southern area as a result of the combination of the plain and upslope wind circulations. The locations of the fronts of the combined circulation for the CNTL, FOREST, and GRASS are the same, about at the southern foot of Limu Mountain. The location of the front for DESERT is about 10 km southward, but the boundary layer for DESERT is higher than for the other three experiments, which is conducive to the development and maintenance of the circulation. Unlike the other directions, the boundary layer height remains at a high level over the northern plain at 17:00 LST. The penetration distance of the plain wind over the northern plain is 5 km further for FOREST than for the others.

In summary, among the four experiments, the valley wind circulation is the strongest for FOREST, which is characterized by further inland penetration, a deeper valley–wind depth, and a larger velocity and vertical extent of updraft motion. In contrast, the valley breeze circulation is the weakest for DESERT, but its duration is the longest. The circulation for GRASS shows little difference from that for the CNTL, but the upslope wind circulation is slightly weakened. This result is contrary to the findings of Miao et al. [30] and Kala et al. [34], who found that the lower soil moisture caused by changes in land cover leads to an enhanced sea breeze circulation, which is characterized by a stronger, deeper, and more penetrative sea breeze; however, it is consistent with the results of Yu et al. [35] showing that reforestation results in an enhanced valley wind circulation. This also indicates that the impacts of land cover changes on the local circulation may vary in different regions, which may be related to the differences in surface energy partitioning caused by the geographical location (e.g., latitude and distance from the coastline) [36,37], size and pattern of land use change [38,39], season [40], and climate [41].

5.3. Mean Wind Field

To further understand the impacts of land cover changes on the circulation as a whole, Figures 13 and 14 show the evolution of the mean horizontal and vertical wind velocity values averaged over the mountain area (the rectangular area marked in Figure 2b). After the area covered by uniform forest (Figure 13b), a noticeable decrease in wind speed occurred in the lowest 100 m ASL. This is due to the larger friction and barrier effects for FOREST as compared with the CNTL. For GRASS (Figure 13c), there is no significant change, except the overall wind speed increases within 0.1–0.6 km ASL slightly. Similarly, for DESERT (Figure 13d), the wind speed increases significantly in the lower boundary layer because of the weakening of vegetation blocking and friction. Interestingly, the increase is more prominent during 17:00–22:00 LST, with the peak being greater than 0.8 m/s and the extent being roughly equal to the boundary layer height. This could be explained by the existence of a stronger valley wind circulation during this period for DESERT.

For the CNTL (Figure 14a), the updraft appears at about 10:00 LST and at up to 1 cm/s at 12:00 LST. Then, the ascending speed increases rapidly, peaking with a magnitude of 4 cm/s at the height of 0.8 km ASL at 14:00–16:00 LST. After 16:00 LST, the updraft gradually decreases at a rate of 1 cm$\cdot$s^{-1}/h. At the same time, the downdraft continues to strengthen and extend downwards. By 22:00 LST, the study area is controlled by the downdraft, with a maximum speed appearing at about 1.1 km ASL, about 0.5 km above the boundary layer height. For FOREST (Figure 14b), the intensity and vertical extension of the updraft are larger, and the center of the updraft is also higher during the daytime. For GRASS

(Figure 14c), the distribution pattern is similar to the CNTL, but the downdraft weakens slightly at night. For DESERT (Figure 14d), showing an opposite pattern to FOREST before 15:00 LST, the intensity and vertical extension of the updraft weakens and the center is lower. However, after 15:00 LST, the ascending motion for DESERT turns out to be the most remarkable among all experiments, and the center of increase is located at around 0.6 km ASL. It is noteworthy that the variation range of the updraft is basically within 1.2 km ASL due to the lower boundary layer height, which suppresses the ascending branch of the valley wind circulation. The above analyses are consistent with those shown in the vertical cross-sections (Figures 9–12), further proving the impacts of the three land cover conditions on the valley circulations.

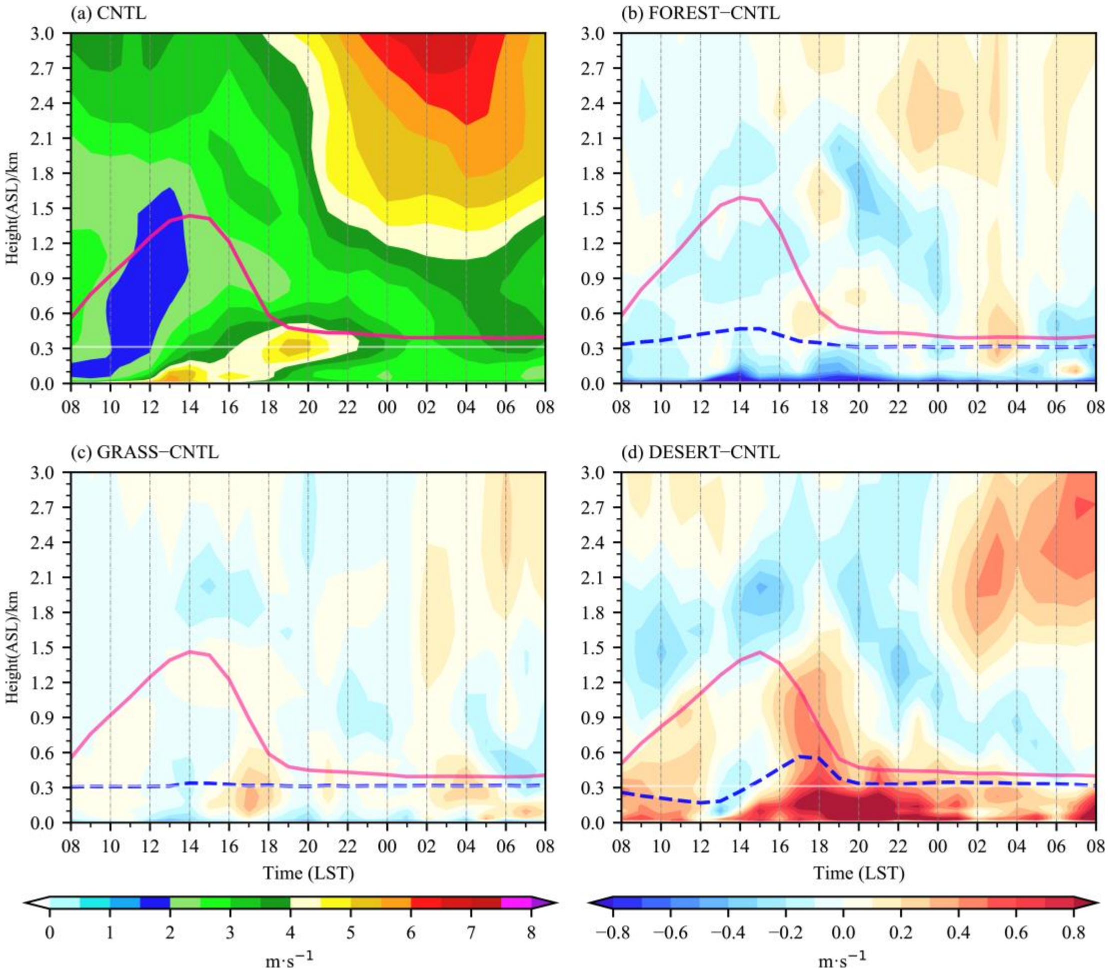

Figure 13. Diurnal variations in (**a**) simulated averaged horizontal wind speed and planetary boundary layer height in the mountain area of the CNTL and (**b**–**d**) the differences between the three sensitivity experiments and the CNTL. The red solid line indicates the boundary layer height, the blue dotted line shows the difference of the boundary layer height between the three sensitivity experiments and the CNTL, and the white straight line indicates the average height of the mountainous area.

5.4. Possible Impact Mechanism

Land use changes play a key role in partitioning the surface energy by modifying land surface parameters such as the albedo, soil thermal conductivity, emissivity, roughness length, and leaf area index. Therefore, the possible mechanism of impact of the land cover changes on the mountain circulation is explored from the perspectives of the radiation and energy balance. Figure 15 compares the diurnal variations in sensible heat, latent heat, and ground heat fluxes averaged over the mountain area between sensitivity and control experiments. For FOREST, both the sensible and latent heat fluxes increase in the daytime due to the lower surface albedo and higher net radiation [42]. The increase in sensible heat flux is more prominent, with an average of 42.6 W/m^2 at 12:00–14:00 LST. For GRASS, the diurnal heat fluxes nearly follow those for the CNTL, with only a slight decrease in the sensible heat and latent heat fluxes during the daytime.

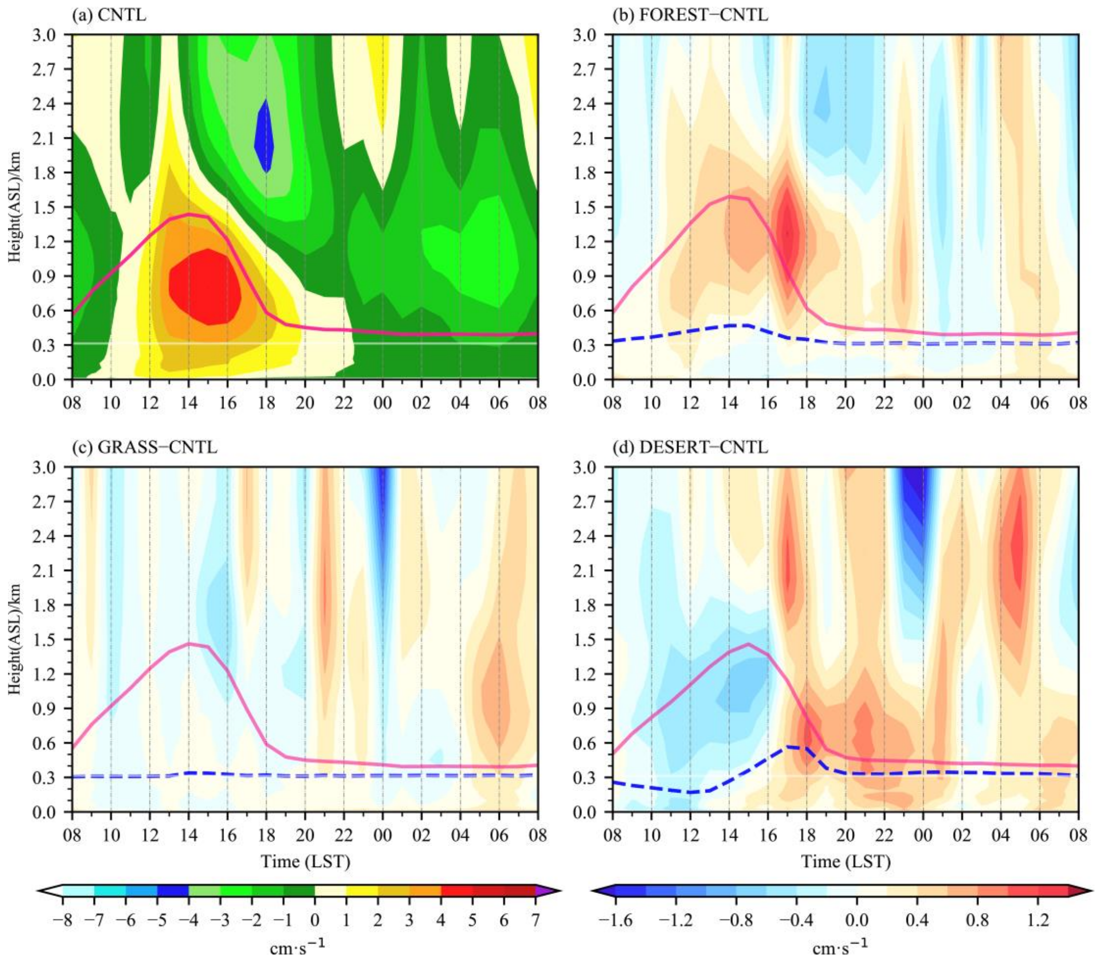

Figure 14. Diurnal variations in (**a**) simulated averaged vertical wind speed in the mountain area of the CNTL and (**b**–**d**) the differences between the three sensitivity experiments and the CNTL.

For DESERT, the latent heat flux decreases significantly because of there being less vegetation and less evapotranspiration, which reaches 287.4 W/m^2 at 13:00 LST. The net radiation is mainly partitioned into sensible heat and soil heat fluxes. The response of the heat fluxes exhibits a distinct change compared to the CNTL, and the change varies with time. For example, in the first half of the valley breeze period (10:00–15:00 LST), the sensible heat flux decreases and the difference between DESERT and the CNTL reaches 51.1 W/m^{-2} at 11:00 LST. In addition, the ground heat flux increases significantly, resulting in a difference of 137.3 W/m^2 at 12:00 LST. This is because the soil thermal conductivity in the Noah land surface model declines exponentially with the vegetation cover fraction [35] and greater ground heat storage capacity for DESERT. In the second half of the valley wind period (16:00–21:00 LST), however, the previously stored ground heat flux starts to release and the sensible heat flux increases, as also shown by Wang et al. [20]. This suggests that more energy is transported into the atmosphere at this period for DESERT.

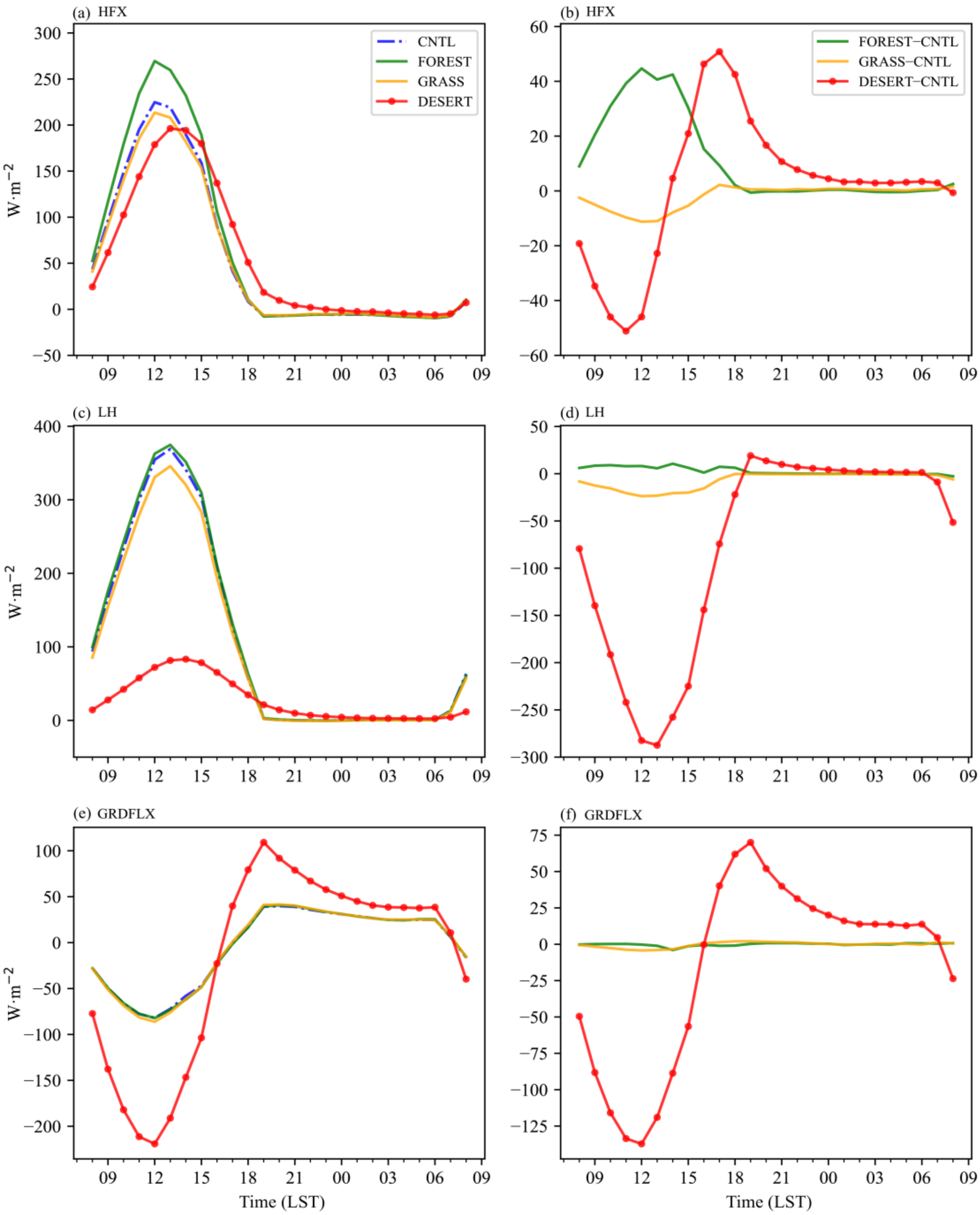

Figure 15. Diurnal variations in simulated averaged heat fluxes in the mountain area for the four experiments (**left**) and the differences between the three sensitivity experiments and the CNTL (**right**): (**a**,**b**) sensible heat flux, (**c**,**d**) latent heat flux and (**e**,**f**) ground heat flux.

After the change in surface energy partitioning, the spatial distribution of the temperature is eventually changed through feedback between the land surface and the atmosphere. Figures 16 and 17 present the evolutions of 2 m potential temperature at different altitudes, temperatures, and boundary layer heights averaged over the mountain area, respectively. The differences among the four experiments mainly occur in the daytime as a result of the different responses of underlying vegetation surfaces to downward solar radiation forcing [43].

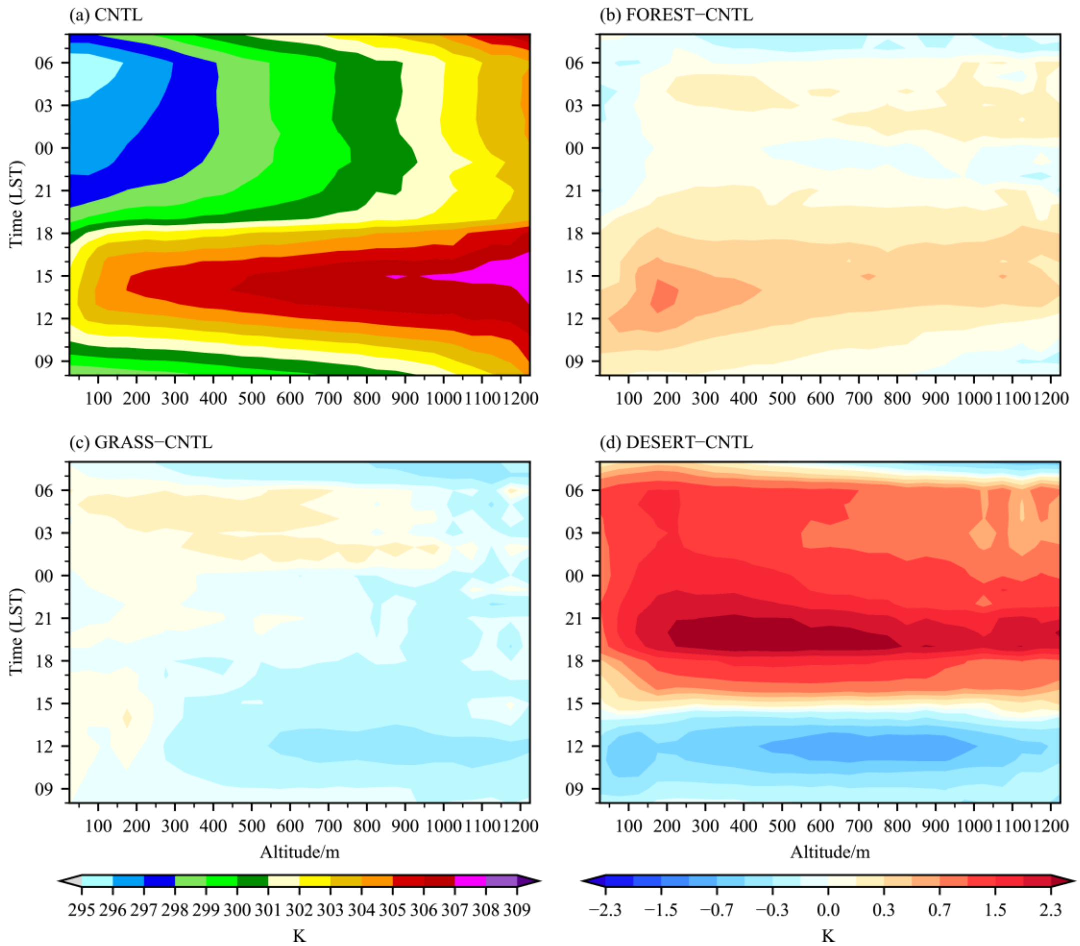

Figure 16. Diurnal variations in (**a**) simulated averaged 2 m potential temperature over mountainous areas with different altitudes for the CNTL and (**b**–**d**) the differences between the three sensitivity experiments and the CNTL.

As shown for the CNTL (Figure 16a), the horizontal potential temperature gradient increases first on the mountain top after sunrise due to the air parcels over the mountain are heating faster than the surrounding air. In the early afternoon, the temperature reaches a maximum, and the high thermal gradient area moves to low-elevation parts below 200 m, indicating the rapid development of the plain wind. For FOREST (Figure 16b), the potential temperature increases during the day, and the increase is more obvious over the plain below 400 m, which coincides with the area with a larger land cover change. As a result, an increase in the horizontal potential temperature gradient is shown in the plain. Moreover, the boundary layer is mainly warmed up during the daytime and the warming reaches up to 0.5 °C, while it mainly cools down above 1.5 km ASL, with a maximum cooling of 0.4 °C (Figure 17b). This structure destabilizes the atmosphere, so the boundary layer height for FOREST is about 200 m higher than that for the CNTL at around 15:00 LST. Yu et al. [35] and Yang et al. [44] also found that reforestation leads to a decrease and increase in the land and near-surface temperatures. They further pointed out that the surface exchange coefficient increases with the roughness, meaning the forest area transports heat more efficiently upward to the atmosphere due to the stronger turbulent mixing associated with the larger surface exchange coefficient.

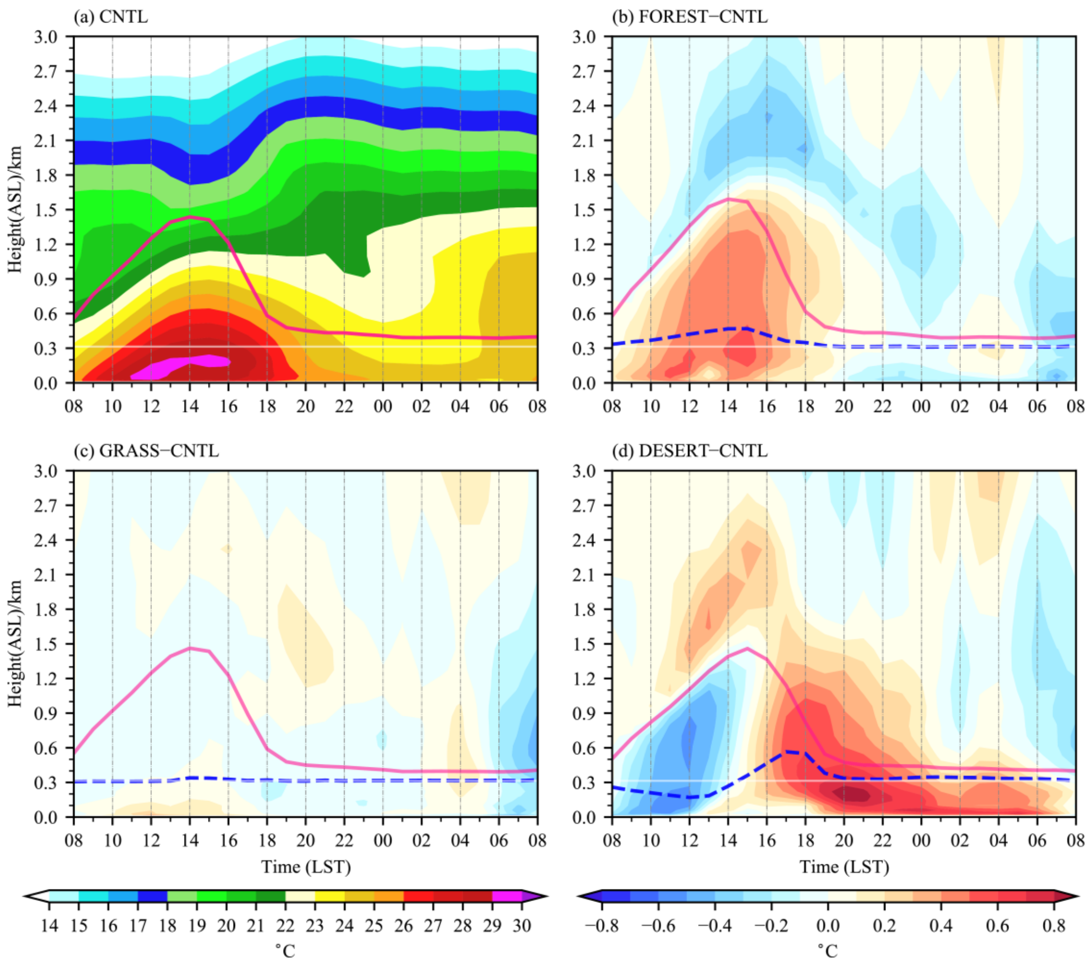

Figure 17. Diurnal variations in (**a**) simulated averaged temperature in the mountain area of the CNTL and (**b**–**d**) the differences between the three sensitivity experiments and the CNTL.

For GRASS (Figures 16c and 17c), small changes in temperature both in the horizontal and vertical directions and a corresponding small change in boundary layer height are present, which are consistent with the small changes in surface heat fluxes. For DESERT (Figures 16d and 17d), the characteristics of the temperature changes are also similar to the surface heat fluxes changes. The near-surface potential temperature decreases in the early valley wind period (10:00–15:00 LST) and increases in the late period (16:00–21:00 LST), and the areas with larger changes are located at altitudes of 400–1000 m and 200–800 m, respectively, resulting in stronger and weaker horizontal potential temperature gradients in the early and later stages. This phenomenon is also shown in the vertical direction. In the early stage (10:00–15:00 LST), the temperature increases in the lower atmosphere, while showing an opposite trend for the higher counterpart. In the later stage (16:00–21:00 LST), the pattern is to the contrary. Therefore, the atmosphere is more stable in the early stage and more unstable in the later stage, accompanied by a lower boundary layer height earlier and a higher height later.

Comparing the horizontal potential temperature gradient and boundary layer structure with the valley wind circulation for the three sensitivity experiments, it can be seen that the changes are very consistent. Specifically, for FOREST, the horizontal potential temperature gradient in the daytime is larger and the boundary layer height is higher. As a result, the valley wind circulation is stronger. For DESERT, the horizontal potential temperature gradient and boundary layer height decrease before 15:00 LST and increase after 15:00 LST. Therefore, the valley wind circulation weakens in the early stage and strengthens in the later stage, resulting in the longest duration of the circulation.

6. Conclusions

In this study, the WRF-ARW (V4.0) was used to simulate a typical case of mountain circulation over the complex terrain in south–central Hainan Island on 1 May 2020. Through three sensitivity experiments with the vegetation types replaced by evergreen broadleaf forest, grass, and bare soil areas, the impacts of land cover changes on the mountain circulation and the possible mechanism were discussed. The major findings were revealed as follows:

1. The vegetation can strengthen the friction and blocking effects that dominate the near-surface wind speed. Among the three sensitivity experiments, the near-surface wind speed was the lowest for FOREST followed by GRASS, and the highest for DESERT, while DESERT showed the most obvious change compared to the CNTL. The valley wind for DESERT was characterized by a 2 m/s stronger speed at 16:00–18:00 LST and a 2 h longer duration. Concurrently, when the water body of the Songtao Reservoir was covered by vegetation, the convergence of the near-surface airflow strengthened due to the weakening of the lake breeze;
2. For all experiments, the valley wind circulation was the strongest for FOREST, with a larger horizontal and vertical extent, and the updraft extended higher. The results for GRASS were similar to that of the CNTL. Opposite to FOREST, the valley breeze circulation was the weakest for DESERT, but it had the longest duration as well as the strongest updraft in the late afternoon;
3. The land cover change affects the surface net radiation and energy partitioning, which in turn alters the spatial distribution of temperature (i.e., the horizontal potential temperature gradient and boundary layer stability). As a result, the structure and evolution of the mountain circulation are affected. Specifically, for FOREST both the sensible and latent fluxes increased in the daytime, especially the sensible heat flux. This led to a larger horizontal potential temperature gradient and a higher boundary layer in the daytime, resulting in a stronger valley wind circulation. Compared with the CNTL, the heat fluxes for GRASS changed little, and the same was true for the changes in circulation. For DESERT, the net radiation was mainly partitioned into sensible and soil heat fluxes. The sensible heat flux decreased and soil heat flux increased significantly before 15:00 LST, while the heat stored in the soil started to release and the sensible heat flux increased after 15:00 LST, resulting in a decrease in the horizontal potential temperature gradient and boundary layer height before 15:00 LST and an increase afterward. Therefore, the valley wind circulation weakened in the early stage and was enhanced in the late stage.

In the future, with the construction of the tropical rainforest national park in the mountain area, the forest coverage area of Hainan Island will continue to expand. Some previous studies [21,45] based on multi-year averaged observations and numerical simulations have shown that the diurnal precipitation in Hainan Island is closely related to the local circulation. Therefore, we preliminarily speculate that due to the enhanced mountain circulation, the expansion of the forest area is likely to lead to an increase in precipitation intensity in the mountain area of Hainan Island, which has favorable water vapor conditions. Notably, the impacts of land cover changes on the mountain circulation may vary with the season, weather, background wind, and other factors. More typical experiments under different conditions need to be conducted to increase the confidence in our findings.

Author Contributions: J.M. designed this study. B.W. conducted the numerical experiments, analyzed the data, and drafted the manuscript under J.M.'s supervision and guidance. J.M. and W.F. revised the manuscript. W.F. acquired the funding. All authors have read and agreed to the published version of the manuscript.

Funding: This study was supported by Hainan Provincial Natural Science Foundation of China (Grant No. 422RC803).

Institutional Review Board Statement: Not applicable.

Informed Consent Statement: Not applicable.

Data Availability Statement: The datasets generated and analyzed during the current study are available from the corresponding author on reasonable request.

Acknowledgments: The two anonymous reviewers are greatly thanked for their valuable comments and suggestions to improve the manuscript.

Conflicts of Interest: The authors declare no conflict of interest.

References

1. Zardi, D.; Whiteman, C.D. Diurnal mountain wind systems. In *Mountain Weather Research and Forecasting: Recent Progress and Current Challenges*; Chow, F.K., De Wekker, S.F.J., Snyder, B.J., Eds.; Springer: Dordrecht, The Netherlands, 2013; pp. 35–119.
2. Miao, Y.C.; Liu, S.H.; Zheng, Y.J.; Wang, S.; Chen, B.C. Numerical study of the effects of topography and urbanization on the local atmospheric circulations over the Beijing-Tianjin-Hebei, China. *Adv. Meteorol.* **2015**, *2015*, 397070. [CrossRef]
3. Yang, X.Y.; Lu, Y.Q.; Ma, Y.M.; Wen, J. Summertime thermally-induced circulations over the Lake Nam Co region of the Tibetan Plateau. *J. Meteorol. Res.* **2015**, *29*, 305–314. [CrossRef]
4. Ganbat, G.; Baik, J.J.; Ryu, Y.H. A numerical study of the interactions of urban breeze circulation with mountain slope winds. *Theor. Appl. Climatol.* **2015**, *120*, 123–135. [CrossRef]
5. Wang, J.; Zhang, L.; Bao, J.; Cao, X.J.; Zhang, B.D.; Zhou, Z.Y. Comparative analysis of mountain-valley wind circulation characteristics over semi-arid areas nearby Lanzhou. *J. Arid Meteor.* **2012**, *30*, 169–177.
6. Weckwerth, T.M.; Bennett, L.J.; Jay Miller, L.; Van Baelen, J.; Di Girolamo, P.; Blyth, A.M.; Hertneky, T.J. An observational and modeling study of the processes leading to deep, moist convection in complex terrain. *Mon. Weather Rev.* **2014**, *142*, 2687–2708. [CrossRef]
7. Miao, Y.C.; Hu, X.M.; Liu, S.H.; Qian, T.; Xue, M.; Zheng, Y.; Wang, S. Seasonal variation of local atmospheric circulations and boundary layer structure in the Beijing-Tianjin-Hebei region and implications for air quality. *J. Adv. Model. Earth Syst.* **2015**, *7*, 1602–1626. [CrossRef]
8. Hari Prasad, K.B.R.R.; Srinivas, C.V.; Rao, T.N.; Naidu, C.V.; Baskaran, R. Performance of WRF in simulating terrain induced flows and atmospheric boundary layer characteristics over the tropical station Gadanki. *Atmos. Res.* **2017**, *185*, 101–117. [CrossRef]
9. Bei, N.F.; Zhao, L.N.; Wu, J.R.; Li, X.; Feng, T.; Li, G. Impacts of sea-land and mountain-valley circulations on the air pollution in Beijing-Tianjin-Hebei (BTH): A case study. *Environ. Pollut.* **2018**, *234*, 429–438. [CrossRef]
10. Zängl, G. A reexamination of the valley wind system in the Alpine Inn Valley with numerical simulations. *Meteorol. Atmos. Phys.* **2004**, *87*, 241–256. [CrossRef]
11. Pielke, R.A. Influence of the spatial distribution of vegetation and soils on the prediction of cumulus convective rainfall. *Rev. Geophys.* **2001**, *39*, 151–177. [CrossRef]
12. Pielke, R.A.; Pitman, A.; Niyogi, D.; Mahmood, R.; McAlpine, C.; Hossain, F.; Goldewijk, K.K.; Nair, U.; Betts, R.; Fall, S.; et al. Land use/land cover changes and climate: Modeling analysis and observational evidence. *WIREs Clim. Chang.* **2011**, *2*, 828–850. [CrossRef]
13. Cao, Q.; Liu, Y.; Georgescu, M.; Wu, J. Impacts of landscape changes on local and regional climate: A systematic review. *Landsc. Ecol.* **2020**, *35*, 1269–1290. [CrossRef]
14. Tian, Y.; Miao, J.F. Overview of mountain-valley breeze studies in China. *Meteor. Sci. Technol.* **2019**, *47*, 41–51.
15. Zhang, Y.C. Numerical experiments of the effects of vegetation of mountain-valley wind circulation. *Sci. Meteor. Sin.* **1995**, *15*, 245–253.
16. Gross, G. Some effects of deforestation on nocturnal drainage flow and local climate—A numerical study. *Bound.-Lay. Meteorol.* **1987**, *38*, 315–337. [CrossRef]
17. Chu, P.C.; Chen, Y.C.; Lu, S.H. Afforestation for reduction of NOX concentration in Lanzhou China. *Environ. Int.* **2008**, *34*, 688–697. [CrossRef]
18. Letcher, T.W.; Minder, J.R. The simulated impact of the snow albedo feedback on the large-scale mountain–plain circulation east of the Colorado Rocky Mountains. *J. Atmos. Sci.* **2018**, *75*, 755–774. [CrossRef]
19. Wang, D.; Miao, J.F.; Tan, Z.M. Impacts of topography and land cover change on thunderstorm over the Huangshan (Yellow Mountain) area of China. *Nat. Hazards* **2013**, *67*, 675–699. [CrossRef]
20. Wang, D.; Miao, J.F.; Zhang, D.L. Numerical simulations of local circulation and Its response to land cover changes over the Yellow Mountains of China. *J. Meteorol. Res.* **2015**, *29*, 667–681. [CrossRef]
21. Liang, Z.M.; Wang, D.H.; Liu, Y.; Cai, Q.B. A numerical study of the convection triggering and propagation associated with sea breeze circulation over Hainan Island. *J. Geophys. Res.-Atmos.* **2017**, *122*, 8567–8592. [CrossRef]
22. Zhu, L.; Bai, L.Q.; Chen, G.X.; Sun, Y.Q.; Meng, Z.Y. Convection initiation associated with ambient winds and local circulations over a tropical island in south China. *Geophys. Res. Lett.* **2021**, *48*, e2021GL094382. [CrossRef]
23. Wang, Y.H.; Miao, J.F.; Cai, Q.B. Numerical simulation of the 3-D structure of sea breezes over the Hainan Island. *J. Trop. Meteor.* **2016**, *32*, 109–124.

24. Han, F.R.; Miao, J.F.; Feng, W. A numerical study of sea breeze circulation under cloudy conditions over Hainan Island. *Trans. Atmos. Sci.* **2017**, *40*, 778–790.
25. Huang, Q.Q.; Cai, X.H.; Song, Y.; Kang, L. A numerical study of sea breeze and spatiotemporal variation in the coastal atmospheric boundary layer at Hainan Island, China. *Bound.-Lay. Meteorol.* **2016**, *161*, 543–560. [CrossRef]
26. Yang, Q.Y.; Miao, J.F.; Wang, Y.H. A numerical study of impact of topography on sea breeze circulation over the Hainan Island. *Acta Oceanol. Sin.* **2017**, *39*, 24–43.
27. Wang, L.Z.; Miao, J.F.; Guan, Y.P. Numerical simulation of impact of topography of Hainan Island on structure of local sea breeze circulation under cloudy weather. *Trans. Atmos. Sci.* **2020**, *43*, 322–335.
28. Liang, Z.M.; Wang, D.H. Sea breeze and precipitation over Hainan Island. *Q. J. Roy. Meteor. Soc.* **2017**, *143*, 137–151. [CrossRef]
29. Zhang, C.W.; He, J.J.; Lai, X.; Liang, T.; Liu, Y.L.; Yang, W.; Che, H.Z.; Gong, S.L. Impacts of high-resolution land surface data on meteorological field simulation over Hainan. *Plateau Meteor.* **2022**, *41*, 775–789.
30. Miao, J.F.; Kroon, L.J.M.; Vilà-Guerau de Arellano, J.; Holtslag, A.A.M. Impacts of topography and land degradation on the sea breeze over eastern Spain. *Meteorol. Atmos. Phys.* **2003**, *84*, 157–170. [CrossRef]
31. Jia, C.H.; Dou, J.J.; Miao, S.G.; Wang, Y.C. Analysis of characteristics of mountain-valley winds in the complex terrain area over Yanqing-Zhangjiakou in the winter. *Acta Meteor. Sin.* **2019**, *77*, 475–488.
32. Cheng, F.Y.; Hsu, Y.C.; Lin, P.L.; Lin, T.H. Investigation of the effects of different land use and land cover patterns on mesoscale meteorological simulations in the Taiwan area. *J. Appl. Meteorol. Clim.* **2013**, *52*, 570–587. [CrossRef]
33. Tian, Y.; Miao, J.F. A numerical study of mountain-plain breeze circulation in eastern Chengdu, China. *Sustainability* **2019**, *11*, 2821. [CrossRef]
34. Kala, J.; Lyons, T.J.; Abbs, D.J.; Nair, U.S. Numerical simulations of the impacts of land-cover change on a southern sea breeze in south-west western Australia. *Bound.-Lay. Meteorol.* **2010**, *135*, 485–503. [CrossRef]
35. Yu, Y.; He, J.J.; Zhao, S.P.; Liu, N.; Chen, J.B.; Mao, H.J.; Wu, L. Numerical simulation of the impact of reforestation on winter meteorology and environment in a semi-arid urban valley, Northwestern China. *Sci. Total Environ.* **2016**, *569*, 404–415. [CrossRef] [PubMed]
36. Wang, X.M.; Chen, F.; Wu, Z.Y.; Zhang, M.; Tewari, M.; Guenther, A.; Wiedinmyer, C. Impacts of weather conditions modified by urban expansion on surface ozone: Comparison between the Pearl River Delta and Yangtze River Delta Regions. *Adv. Atmos. Sci.* **2009**, *26*, 962–972. [CrossRef]
37. You, C.; Fung, J.C.H.; Tse, W.P. Response of the sea breeze to urbanization in the Pearl River Delta Region. *J. Appl. Meteorol. Clim.* **2019**, *58*, 1449–1463. [CrossRef]
38. Saad, S.I.; da Rocha, H.R.; Silva Dias, M.A.F.; Rosolem, R. Can the deforestation breeze change the rainfall in Amazonia? A case study for the BR-163 highway region. *Earth Interact.* **2010**, *14*, 1–25. [CrossRef]
39. Papangelis, G.; Tombrou, M.; Dandou, A.; Kontos, T. An urban "green planning" approach utilizing the Weather Research and Forecasting (WRF) modeling system. A case study of Athens, Greece. *Landscape Urban Plan.* **2012**, *105*, 174–183. [CrossRef]
40. Lejeune, Q.; Davin, E.L.; Guillod, B.P.; Seneviratne, S.I. Influence of Amazonian deforestation on the future evolution of regional surface fluxes, circulation, surface temperature and precipitation. *Clim. Dynam.* **2015**, *44*, 2769–2786. [CrossRef]
41. Shepherd, J.M.; Carter, M.; Manyin, M.; Messen, D.; Burian, S. The impact of urbanization on current and future coastal precipitation: A case study for Houston. *Environ. Plann. B* **2010**, *37*, 284–304. [CrossRef]
42. Takahashi, A.; Kumagai, T.; Kanamori, H.; Fujinami, H.; Hiyama, T.; Hara, M. Impact of tropical deforestation and forest degradation on precipitation over Borneo island. *J. Hydrometeorol.* **2017**, *18*, 2907–2922. [CrossRef]
43. Zhang, C.L.; Chen, F.; Miao, S.G.; Li, Q.C.; Xia, X.A.; Xuan, C.Y. Impacts of urban expansion and future green planting on summer precipitation in the Beijing metropolitan area. *J. Geophys. Res.-Atmos.* **2009**, *114*, D02116. [CrossRef]
44. Yang, S.P.; Lv, S.H.; Chen, Y.C.; Ao, Y.H.; Yu, Y. Simulation of afforestation effect on urban boundary layer structure of valley city in winter. *J. Desert. Res.* **2010**, *30*, 691–698.
45. Zhu, L.; Meng, Z.; Zhang, F.; Markowski, P.M. The influence of sea- and land-breeze circulations on the diurnal variability in precipitation over a tropical island. *Atmos. Chem. Phys.* **2017**, *17*, 13213–13232. [CrossRef]